Nanoscale

Deep Learning-Driven Forward and Inverse Design of Nanophotonic Nanohole Arrays: Streamlining Design for Tailored Optical Functionalities and Enhancing Accessibility

Journal:	*Nanoscale*
Manuscript ID	NR-ART-07-2024-003081
Article Type:	Paper
Date Submitted by the Author:	25-Jul-2024
Complete List of Authors:	Jahan, Tasnia ; University of Dhaka Faculty of Engineering and Technology, Electrical and Electronic Engineering Dash, Tomoshree; University of Dhaka Faculty of Engineering and Technology, Electrical and Electronic Engineering Arman, Shifat ; University of Dhaka Faculty of Engineering and Technology, Electrical and Electronic Engineering Inum, Reefat ; UC Santa Cruz Islam, Sharnali; University of Dhaka Faculty of Engineering and Technology, Electrical and Electronic Engineering; University of Dhaka Jamal, Lafifa ; University of Dhaka Faculty of Engineering and Technology, Electrical and Electronic Engineering Yanik, Ahmet Ali; University of California Santa Cruz, Electrical and Computer Engineering; California Institute for Quantitative Biosciences, Habib, Ahsan; University of Dhaka Faculty of Engineering and Technology, Electrical and Electronic Engineering

Journal Name

ARTICLE TYPE

Cite this: DOI: 00.0000/xxxxxxxxxx

Deep Learning-Driven Forward and Inverse Design of Nanophotonic Nanohole Arrays: Streamlining Design for Tailored Optical Functionalities and Enhancing Accessibility†

Tasnia Jahan[a], Tomoshree Dash[a], Shifat E. Arman[b], Reefat Inum [c], Sharnali Islam[a], Lafifa Jamal[a], Ahmet Ali Yanik[c] and Ahsan Habib* [a,d]

Received Date
Accepted Date

DOI: 00.0000/xxxxxxxxxx

In nanophotonics, nanohole arrays (NHAs) are periodic arrangements of nanoscale apertures in thin films, offering versatile optical functionalities essential for various applications. Fully exploring NHAs' optical properties and optimizing performance demands understanding both materials and geometric parameters, posing a computational challenge due to numerous potential combinations. Efficient computational modeling is crucial for overcoming this challenge and optimizing NHA-based device performance. Traditional approaches rely on time-consuming numerical simulation processes for device design and optimization. However, employing a deep learning approach offers an efficient solution for NHAs design. In this work, a deep neural network within the forward modeling framework accurately predicts the optical properties of NHAs, utilizing device structure data such as periodicity and hole radius as model inputs. Additionally, we compare three deep learning-based inverse modeling approaches—fully connected neural network, convolutional neural network, and tandem neural network—to provide approximate solutions for NHA structures based on their optical responses. Once trained, the DNN precisely predicts the desired result in milliseconds, enabling repeated use without wasting computational resources. Leveraging a comprehensive dataset generated through finite-difference time-domain (FDTD) simulations, the models are trained with over 6000 samples. The forward model accurately predicts transmission spectra, while the inverse model reliably infers material attributes, lattice geometries, and structural parameters from the spectra. Notably, the forward model achieves remarkable accuracy, with an average Mean Squared Error (MSE) of 2.44×10^{-4} in predicting transmission spectra. Furthermore, the inverse design demonstrates high accuracy with deviations of less than 1.5 nm for critical geometrical parameters. For experimental verification, gold nanohole arrays are fabricated using deep UV lithography. Validation against experimental data underscores the models' robustness and precision. These findings indicate that the trained DNN models offer accurate predictions, reflecting the optical behavior of nanohole arrays.

1 Introduction

In 1998, Thomas Ebbesen and colleagues unveiled the extraordinary phenomenon of light transmission through nanohole arrays (NHAs) in two groundbreaking papers.[1,2] These arrays consist of thin metal films perforated with holes ten times smaller than the wavelength of light. These seminal works sparked a revolution in the field of nanophotonics, opening up new possibilities for tailored optical functionalities.[3,3–8] In recent years, the emergence of dielectric NHAs has divided the landscape into two distinct categories: metallic[9] and dielectric.[10] Metallic arrays, with plasmonic resonances resulting from free electrons in metals.[11,12] On the other hand, dielectric arrays offer alternative optical functionalities such as enhanced scattering, diffraction, and waveguiding effects, without supporting strong plasmonic effects. Dielectric metasurfaces have been introduced to address the high losses of

[a] Department of Electrical and Electronic Engineering, University of Dhaka, Dhaka-1000, Bangladesh; E-mail: mahabib@du.ac.bd
[b] Department of Robotics and Mechatronics Engineering, University of Dhaka, Dhaka-1000, Bangladesh
[c] Department of Electrical and Computer Engineering, University of California, Santa Cruz, CA-95064, United States of America
[d] Dhaka University Nanotechnology Center, University of Dhaka, Dhaka-1000, Bangladesh

† Electronic Supplementary Information (ESI) available: [details of any supplementary information available should be included here]. See DOI: 00.0000/00000000.

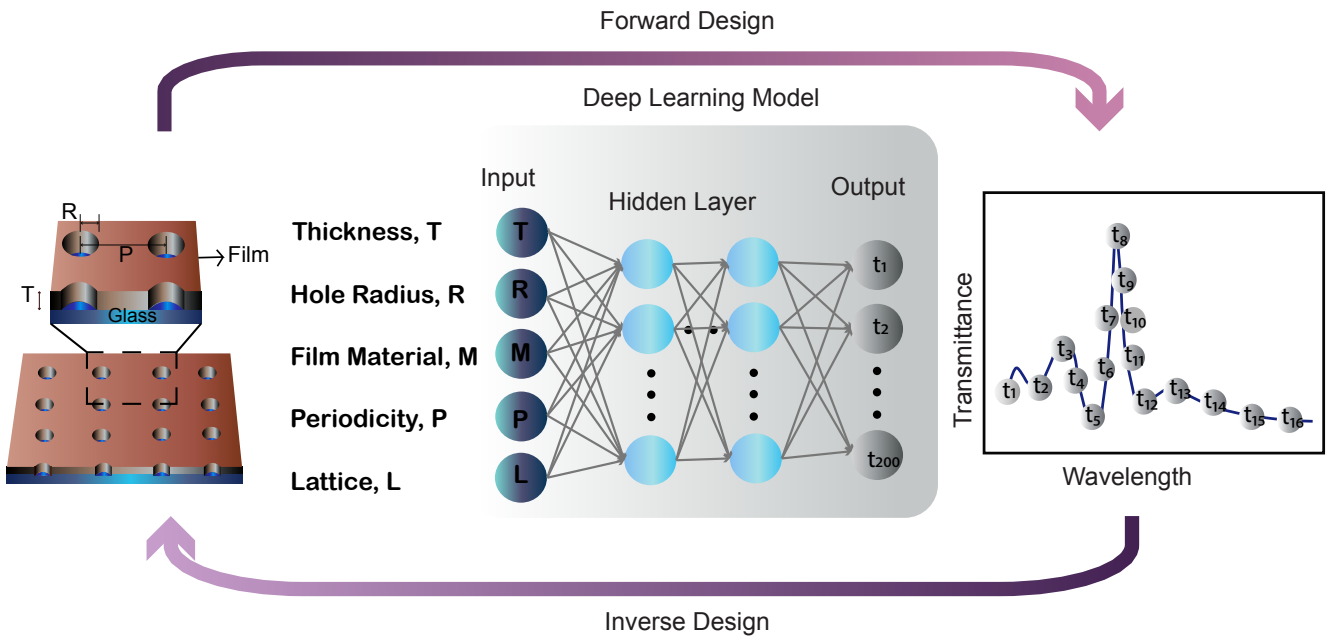

Fig. 1 Spectral data prediction by the deep neural network based on nanohole array parameters: (i) Thickness (T), (ii) Hole Radius (R), (iii) Film Material, (iv) Periodicity, and (v) Lattice. The inverse design can predict these structural parameters from transmission spectra.

metallic arrays, supporting resonances with higher quality factors (Q-factors) for improved performance and reduced losses.[13] Combining the strengths of both types opens new possibilities for enhanced light-matter interactions and tailored optical functionalities. However, designing NHAs using conventional electromagnetic tools can be a time-consuming and challenging process for several reasons. Firstly, the intricate geometries and subwavelength features of NHAs often require computationally expensive simulations, such as finite-difference time-domain (FDTD), which demand substantial computational resources and time. Secondly, generating a design that matches a target spectrum typically involves a trial-and-error approach, requiring multiple iterations of simulations and adjustments of design parameters. This iterative process becomes particularly cumbersome when aiming for specific resonance frequencies or intricate optical functionalities. In addition, conventional methods still require costly simulations even if the wavelength or resonance frequency is known, preventing efficient and streamlined design.

Deep learning, a subset of machine learning, comprises input, output, and hidden layers, enabling neural networks to learn nonlinear relationships between input and output parameters from extensive datasets.[14] In the field of nanophotonics, deep learning has shown immense promise for forward modeling, where it predicts the optical response of a photonic system based on geometric parameters.[15] For instance, Li et al. employed a deep learning algorithm to predict the circular dichroism spectrum of gold NHAs with chiral structures.[16] In another study, Li et al. accurately predicted the magnetic field distribution of nanostructure-based scatterers using deep learning.[17] Conversely, inverse modeling does the opposite, predicting geometrical parameters from optical data.[18] These data-driven approaches offer faster and more cost-effective methods to obtain desired outputs.[19]

A broad spectrum of neural network and machine learning architectures has been rigorously explored to address diverse inverse design challenges in the field of nanophotonics. These challenges encompass a variety of applications, ranging from the inverse design of topological photonics[20], plasmonic waveguides[21], graphene-based metamaterials[22], plasmonic nanostructures[23], to multilayer spherical nanoparticles[24]. At the heart of these inverse models is the objective of deducing structural configurations from target spectra, which are characterized by distinctive peaks and valleys. Convolutional Neural Networks (CNNs) have demonstrated significant promise in extracting salient features from these spectral signatures, facilitating the inverse design of chiral metamaterials[25], plasmonic metasurfaces[26,27], and broadband metasurface absorbers[28]. One of the principal challenges in nanophotonic inverse design is the issue of non-uniqueness, where multiple structural configurations can result in identical optical responses. This problem has been effectively addressed through the deployment of tandem neural networks, which has been applied to the inverse design of multilayer thin films[29], silicon structural colors[30], core-shell nanoparticles[31], and nanophotonic waveguides[32]. Recently, Liu et al. used a bidirectional tandem network to input color and spectrum data directly to predict the structural parameters of Ag NHAs[33]. However, exploring a wider range of materials and lattice structures could make the deep learning method more applicable to designing various NHAs. Additionally, including experimental validation of the designed nanohole arrays would help bridge the gap between theoretical predictions and practical implementation, further proving the robustness of the deep learning approach.

In this work, we utilize deep neural networks to predict the optical properties and structural parameters of NHAs. We start by generating transmission spectra through finite difference time-domain (FDTD) simulations, creating the foundational dataset for training our neural networks. Central to our approach is the development of a forward-modeling neural network designed to accurately predict transmittance based on NHA parameters: (i) thickness (T), (ii) hole radius (R), (iii) film material, (iv) periodicity, and (v) lattice (Figure 1). Furthermore, we explore the efficacy of three neural network architectures—fully connected, convolutional, and tandem networks—in predicting the parameters of nanohole arrays from spectral data. Strategic optimization of hyperparameters significantly enhances model performance, enabling precise and rapid characterization and optimization of NHAs. Our methodology exhibits versatility, extending to five distinct types of NHAs and offering broad applicability in predicting their structure and transmission spectra. Our models demonstrate accuracy through key performance metrics: the forward model has an average mean squared error (MSE) of about 2.44×10^{-4} when predicting transmission spectra. On the other hand, the inverse model shows high precision, with deviations less than 1.5 nm for critical geometric parameters. To validate the practical applicability of our neural network predictions, we fabricate gold on glass nanoholes. The fabricated nanoholes exhibit excellent concordance with the neural network's forecasts, thereby underscoring the reliability and effectiveness of our deep learning-assisted inverse design methodology.

2 Methodologies

2.1 Structure and Dataset Generation

We explored circular nanohole arrays (NHAs) arranged in square and hexagonal patterns. These arrays contained commonly used metals such as gold (Au) and silver (Ag), as well as a dielectric material called hydrogenated amorphous silicon dioxide (a-SiOx:H). These materials demonstrated extensive applicability in a wide range of fields, including bio/chemical sensing, spectroscopy, imaging, and beyond.[34–36] Our study included five combinations of materials and array structures, namely: Au NHA in hexagonal arrangement, Ag NHA in hexagonal arrangement, a-SiOx:H NHA in hexagonal arrangement, Au NHA in square arrangement, and Ag NHA in square arrangement.

Table 1 Materials and Lattice Arrangements

Materials		Lattice Arrangements	
Material	Index	Lattice Arrangement	Index
Au	0	Hexagonal	0
Ag	1	Square	1
a-SiOx:H	2		

For the forward neural network training, we selected key input parameters, comprising film thickness (T), hole radius (R), periodicity (P), film material, and nanohole array lattice arrangement. Systematically varying these parameters within defined ranges, we explored film thickness from 100 nm to 150 nm, hole radius from 50 to 100 nm for hexagonal lattice and 100 to 150 for square lattice, and periodicity from 475 nm to 525 nm, with a step size of 5 nm. Total number of combinations was calculated by multiplying the steps in each parameter: 11 for film thickness, 11 for hexagonal lattice hole radius, 11 for square lattice hole radius, and 5 for the different array types, resulting in a total of 6655 unique combinations. In our training instances, full-wave numerical simulation utilizing the FDTD method was used to calculate the transmittance spectra for various combinations of these three parameters (T, R, and P) across five different types of NHAs. To accurately model the infinite array effect, we implemented periodic boundary conditions in the x and y directions, while perfectly matched layers effectively suppressed reflections at the top and bottom boundaries of the computational domain. The refractive index of a-SiOx:H was 2.4 with an extinction coefficient of 5×10^{-4}.[10] For Au, we used data published by "Johnson and Christy,"[37] and for Ag, we used data published by "Palik"[38]. We benchmarked our FDTD simulations by computing the transmittance spectrum of a square lattice NHA and comparing it with our experimental data (Supplementary Text 1 and Supplementary Figure S1a). Similarly, for a hexagonal lattice NHA, we compared it with the experimental data available in published work (Supplementary Figure S1b)[10]. The experimental spectra were in excellent agreement with our simulations.

Employing a directed plane wave source with an incident electric field magnitude of 1 Vm^{-1} and polarization along the x-axis, our simulations produced comprehensive transmittance spectra, spanning wavelengths from 550 nm to 1100 nm and comprising 200 data points. To assess the diversity of the transmission spectra, we segmented them into five intervals for each type of nanohole array. These intervals were as follows: 0-0.0001, 0.0001-0.001, 0.001-0.01, 0.01-0.1, and 0.1-10. Supplementary Table S1 showed a notable presence of transmission spectra values within each range, indicating a diverse dataset. The final dataset comprised 205 columns and 6655 rows. The first column denoted the NHA structure (hexagonal and square), while the second column indicated the film material. Addressing the inverse problems of predicting material and array arrangement, we assigned numerical values of 0, 1, and 2 to these parameters, as detailed in Table 1. Thus, the first and second columns of the dataset contained the assigned numbers 0, 1, and 0, 1, or 2, respectively. The third, fourth, and fifth columns provided the precise values of thickness, radius, and periodicity. The remaining 200 columns represented transmittance data points specific to distinct wavelength values. Each row corresponded to a unique combination of input parameters and their corresponding transmittance data points, forming a comprehensive training dataset for the forward neural network. Supplementary Text 2 shows the data quality and diversity of our dataset. For inverse prediction, we used the same dataset, using spectral data as input parameters and lattice arrangements, material attributes, film thickness, hole radius, and hole periodicity as output parameters.

2.2 Architecture and Training of Neural Networks

In our deep learning approach, the model underwent essential training, validation, and testing processes to optimize its perfor-

mance, assess generalization, and evaluate predictive capabilities. To ensure balanced representation, we randomly split the dataset, allocating 80% as the training set, 10% for validation, and the remaining 10% for testing. Additionally, to promote consistent and stabilized gradient descent steps, we normalized the structural parameter values before utilizing them as input parameters. Both the forward and inverse models were constructed using the well-established open-source deep learning framework, Keras.[39] In the forward problem, which was predominantly a regression task, we utilized the Mean Squared Error (MSE) as the loss function, defined as:

$$MSE = \frac{1}{n}\sum(t_i^{real} - t_i^{pred})^2 \quad (1)$$

where n was the size of the batch data, t_i^{real} denoted the spectral points, and t_i^{pred} represented the predicted value for the ith sample. We used the Adam optimizer to minimize the loss function with the help of gradient descent, as it allowed for faster convergence on nonlinear datasets. The training dataset was fed into the network with a batch size of 128. The output layer used the linear activation function, and the rectified linear activation function (ReLU) was employed for the dense layers.

In the inverse problem, we solved both classification and regression tasks. We used Sparse Categorical Cross-Entropy as the loss function for classification problems. For the regression problem, which predicted continuous and numeric outputs, we used the Mean Squared Error (MSE) loss function,[27,30,40–42] defined as:

$$MSE = \frac{1}{m}\sum(\bar{y}_i - y_i)^2 \quad (2)$$

where m was the number of training examples, y_i represented the ground truth values, and $\bar{y}_i$ denoted the predicted values. The ReLU activation function was used in the dense layers. In the output layers, the softmax and linear activation functions were used for the classification and regression problems, respectively. Training parameter details are shown in Supplementary Table S2. We evaluated the performance of a fully connected network, convolutional neural network, and tandem neural network architecture tailored for the effective analysis and interpretation of one-dimensional (1-D) spectral data. The architecture of the fully connected network for solving the inverse problem comprised dense layers and was the same as for the forward problem. As the inverse problem was based on 1-D spectral data, our convolutional neural network comprised Conv 1D layers, max-pooling layers, and batch normalization layers.

The tandem neural network was composed of two networks: a trainable inverse network and a pre-trained forward network.[32,43] Together, they worked iteratively to minimize the disparity between targeted and generated transmission spectra, thereby addressing the issue of non-unique solutions. The inverse network, which was subject to training, was designed to predict design parameters starting from a desired transmission spectrum. The forward network, fixed in its parameters (weights and biases), predicted the transmission spectrum given a set of design parameters. Training began with the inverse network receiving a target transmission spectrum as input. It then predicted a set of design parameters that could reproduce this spectrum. These predicted parameters were fed into the pre-trained forward network, generating a reconstructed transmission spectrum. The error between this reconstructed spectrum and the original target spectrum was included as training loss, with the objective of minimizing this error through iterative adjustments to the inverse network's parameters. To mitigate the issue of non-uniqueness—where multiple sets of design parameters could yield similar transmission spectra—the tandem architecture harnessed the forward network's fixed parameters as a guide. By adjusting only the inverse network's parameters, the system converged towards a singular, optimal set of design parameters that aligned with the forward model's predictions.

2.3 Hyperparameter Optimization

Maximizing the performance of neural networks necessitates tuning hyperparameters—diverse parameters affecting the learning process, such as the learning rate, batch size, and the number of hidden layers[44]. This process involves minimizing a loss function by selecting the most appropriate hyperparameters tailored to the specific predictive task at hand. In this study, we used Optuna,[45] an open-source framework for optimizing hyperparameters. We selected three crucial parameters as hyperparameters: the number of hidden layers, the number of nodes, and the learning rate. We also optimized the number of convolutional layers and filters for a 1D CNN. The number of dense layers and nodes in the 1D CNN were optimized as well. We compared the performance between two cost functions: MSE and MAE. To optimize the process, we used the Tree-structured Parzen Estimator (TPE) as a sampler. Using TPE, we started with assumptions about the best hyperparameters. We refined these assumptions based on how different hyperparameters affected model performance. The optimization method began by defining an objective function. This function took hyperparameters as input and returned a score or loss value. For our forward and inverse models, we used Mean Squared Error (MSE) loss values as the objective function. We defined a search space for the TPESampler to explore. This search space included a range of configurations: the number of dense layers (from 1 to 10), the number of nodes (from 100 to 2000), and the learning rate (from 0.0001 to 0.001). For the 1D CNN, we varied the convolutional layers from 1 to 6 and the number of filters among 16, 32, 64, 128, and 256.

2.4 Fabrication of Gold Nanohole Arrays

Gold nanohole arrays in a square lattice arrangement were fabricated using DeepUV photolithography at $\lambda = 248$ nm. The process involved patterning the substrates of 500 μm thick, 100 mm diameter fused silica wafers (UniversityWafer, Inc.; U01-120920-5), which were cleaned with piranha solution (3 : 1 H_2SO_4:H_2O_2) and solvent cleaned in acetone/isopropanol ultrasonic baths. Electron-beam deposition of 5 nm titanium (Ti) and 120 nm gold (Au) layers (Sharon Vacuum Co.) followed. NHAs were patterned using Deep-UV photoresist (Microchem Corp. UV 210GS-0.3) spun to approximately 250 nm thickness, with a bottom anti-reflection layer (Brewer Science Inc. DUV42P-6). The

pattern was exposed with an ASML PAS 5500/300 Deep-UV stepper for 270 nm hole diameter and 475 nm to 525 nm periodicity and developed in AZ 300 MIF Developer (Integrated Micro Materials).

To prevent redeposition of sputtered material onto the photoresist sidewalls during ionbeam etch, the photoresist was etched to produce a slanted sidewall with an Oxygen RIE etch at 10 mT, 200W RF in a Plasmatherm SLR 770. Ion beam etching (Oxford Instruments, Ionfab 300 Plus) was then used to transfer the NHA pattern into the metallic layers using a normal-incidence Argon ion-beam of 150 mA beam current and 500 V beam voltage. Subsequently, the photoresist was removed via dry etching in an oxygen plasma asher (Technics PE II-A). This fabrication method enabled the production of subwavelength nanoholes over the entire wafer in a monolithic process. To protect the sensor surface from debris, the 4-inch wafer was coated with a layer of photoresist (Microchem Corp., UV6-0.8) and diced into 1:5 cm× 1:5 cm chips. The photoresist layer was removed using 5 minutes ultrasonication in an acetone solvent, followed by an isopropyl alcohol (IPA) wash and N_2 dry steps.

3 Result and Discussion

3.1 Deep Learning Model Construction for Nanohole Array Design

In constructing an efficient deep learning model for nanohole array design, we focused on selecting and optimizing key hyperparameters, including the number of layers, the number of nodes per layer, and the learning rate. We use the Tree-structured Parzen Estimator (TPE) method for this optimization. Our optimal forward model includes five dense layers, each with 1080 nodes (Supplementary Figures S2a and S2b. The optimal learning rate is 0.00011. Dropout is employed as a regularization technique in our neural network models, where a fraction of nodes, specifically 20%, are randomly deactivated during the training process. This method enhances the robustness of the model by mitigating the risk of overfitting. By preventing the network from becoming overly reliant on particular nodes, dropout improves the model's generalization capabilities, ensuring better performance on unseen data.[46] The input layer has five nodes representing critical parameters like structural features, material types, and array geometries, while the output layer has 200 nodes to model various transmittance points (Supplementary Figure S3-inset). Supplementary Figure S3 shows the efficacy of our model. The learning curves indicate a rapid initial decrease in MSE for both the training and validation datasets. The training MSE stabilizes at a lower value, demonstrating effective learning, while the slightly higher validation MSE indicates good generalization and robust model performance (Supplementary Figure S3 and Supplementary Text 3).

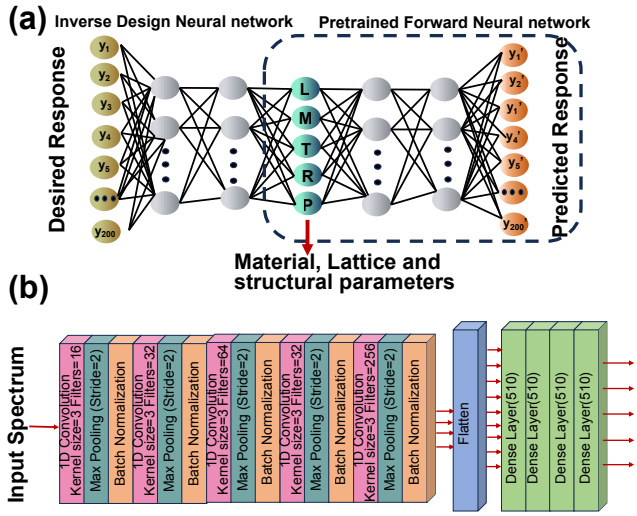

Fig. 2 (a) The architecture of Tandem Neural Network, comprising an inverse network connected to a pre-trained forward network; (b) The architecture of Convolutional Neural Network for inverse design.

Our optimal fully connected inverse network includes six layers, each with 1180 nodes (Supplementary Figures S2c and S2d). The optimal learning rate is 0.000325. The inverse model performs both classification tasks, such as identifying the array's geometry (square or hexagonal) and the materials involved (Au, Ag, or a-SiOx:H), and regression tasks, including predicting hole thickness, radius, and periodicity. For the tandem architecture, this fully connected neural network is placed before the pre-trained forward network, which consists of five dense layers, each containing 1080 nodes (Figure 2a). The optimized hyperparameters of the 1D CNN are presented in Supplementary Table 3. The CNN is composed of five Conv 1D layers with filter numbers of 16, 32, 64, 32, and 256, and dense layers (four layers, each with 510 nodes) (Figure 2b). The optimized learning rate for the 1D CNN is 0.00017. Target spectra with an array size of 1×200 are given input to the first Conv 1D layer. Each Conv 1D layer is followed by a max-pooling layer, and a batch normalization layer. We applied ReLU as the activation function. In Figure S4 and Supplementary Text 3, we present the training losses and validation losses for three inverse models. These losses provide insight into how well our models are learning from the training data over successive epochs.

Following the optimization of our deep learning models, we conduct a detailed evaluation to understand the impact of dataset size on model performance. Supplementary Table S4 presents the performance metrics, including mean absolute error (MAE) and R-squared values, for dataset sizes of 4990 and 6655. The MAE is expressed as $MAE = \frac{1}{n}\sum|\bar{x}_i - x_i|$, where n is the size of the test dataset, x_i represents the ground truth values, and $\bar{x}_i$ denotes the predicted values of structural parameters. A lower MAE value indicates higher accuracy. The results show that increasing the dataset size significantly enhances the model's accuracy and generalization capabilities. For instance, the inverse model (tandem neural network) trained on the larger dataset exhibits the lowest MAE and the highest R-squared values, underscoring the importance of ample training data for achieving optimal performance. Additionally, for forward prediction, the mean squared error (MSE) decreases when the model is trained with a larger dataset, further confirming the benefits of using extensive data. Additionally, we examine the impact of different cost functions on model performance. Supplementary Table S5 presents the MAE

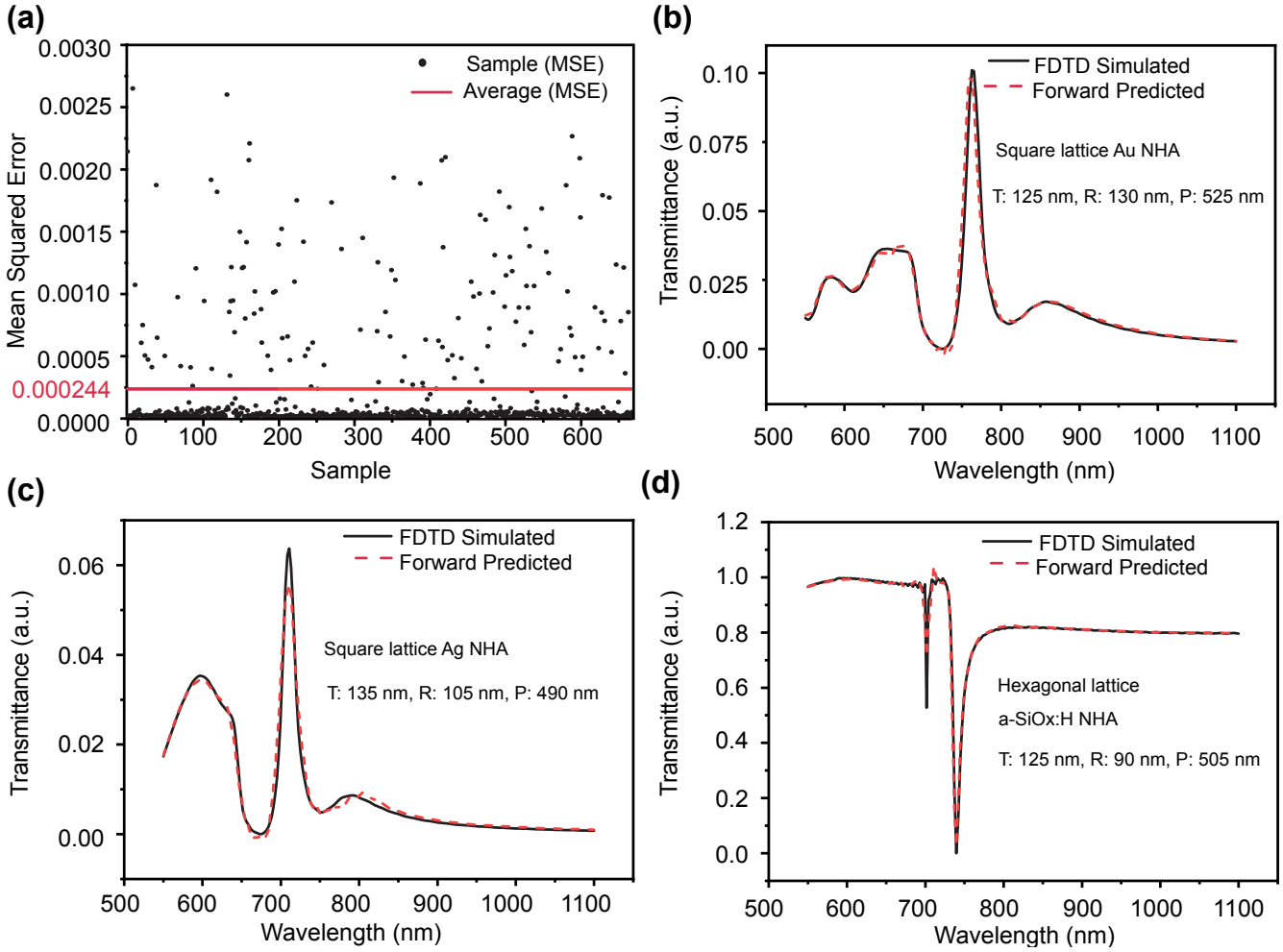

Fig. 3 Mean squared error distribution and forward prediction of NHA transmission spectrum. (a) Distribution of mean squared error (MSE) for 666 samples from the test dataset. The black dots represent the MSE for individual samples, while the red line indicates the average MSE of 0.000244. (b) Comparison of the transmission spectrum calculated from DNN prediction (red dashed line) with numerical simulations (black solid line) for a square lattice with Au film. Design parameters are T: 125 nm, R: 130 nm, P: 525 nm, where thickness, radius, and periodicity are denoted by T, R, and P respectively. (c) Similar comparison for a square lattice with Ag film. Design parameters are T: 135 nm, R: 105 nm, P: 490 nm. (d) Similar comparison for a hexagonal lattice with a-SiOx:H film. Design parameters are T: 125 nm, R: 90 nm, P: 505 nm. In all spectral plots, the DNN-predicted spectra closely match the FDTD-simulated spectra, demonstrating the accuracy of the forward model.

and R-squared values for inverse models, and the MSE for forward models, trained with both MAE and MSE as cost functions. The results highlight the superior performance of using MSE as the cost function for training both inverse and forward models.

3.2 Evaluation of Deep Learning Models for Nanohole Array Design

For evaluating the performance of our forward modeling network, we use data from a test set that the neural network has never trained on. In Figure 3a, we show the distribution of MSE across the test samples. The average MSE, calculated between the predicted and actual transmission spectra of the test dataset, is approximately 2.44×10^{-4} (Figure 3a-red line). To further assess the model, we used a set of dimensional parameters as input for the neural network, generating corresponding transmission spectra. In Figures 3b-3d and Supplementary Figure S5, the dashed red curves represent the transmission spectra predicted by the neural network, while the black curves depict the true transmission spectra simulated by FDTD. Notably, the NN-predicted and FDTD-simulated spectra are highly comparable, essentially overlapping. This alignment in resonant properties underscores the potential applicability of the forward network in plasmonic sensor contexts.

In the inverse prediction, after training the neural networks, we feed the spectra from the test dataset into the networks. The networks then predict the parameters: thickness (T), radius (R), and periodicity (P), and we compare their performances in Figure 4. In Figure 4a, we exhibit the comparison of MAE between the true parameter values and predicted parameter values given by the three networks. The MAE for the tandem network is the lowest, implying it has the highest accuracy. For thickness and radius, the MAE values are below 1.3 nm, while periodicity prediction exhibits an MAE value below 0.6 nm. In Figure 4b, we calculate and compare the R^2 scores for thickness, radius, and periodicity of the three networks. A high R^2 score signifies strong agreement

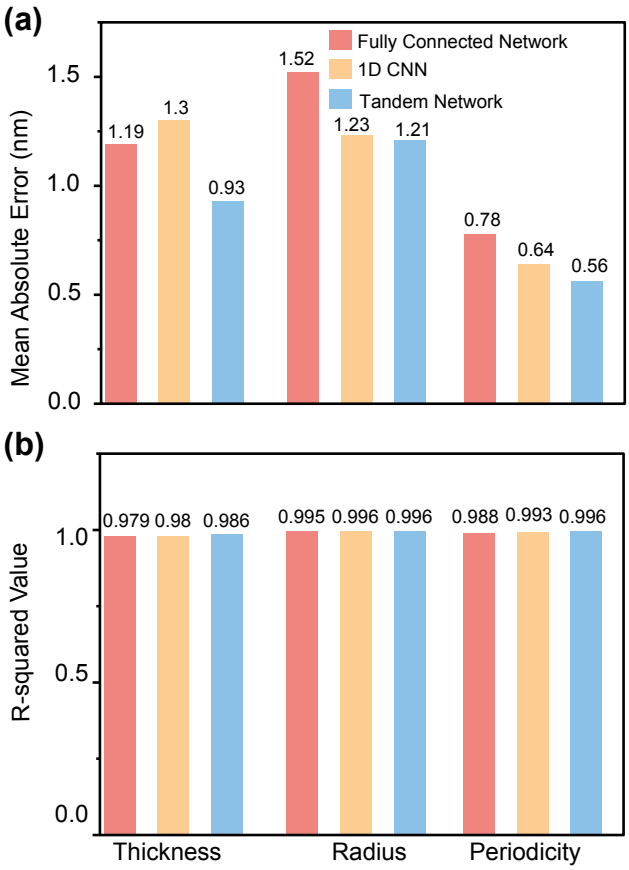

Fig. 4 Performance comparison of different neural network architectures for inverse design of nanohole arrays. (a) Mean Absolute Error (MAE) between true values and predicted values for three different neural network architectures: Fully Connected Network (red), 1D Convolutional Neural Network (yellow), and Tandem Network (blue). The MAE is presented for the prediction of thickness, radius, and periodicity. The Tandem Network shows the lowest MAE for thickness (0.93 nm), and radius (1.21 nm). (b) R-squared (R^2) values for the same three neural network architectures. Higher R^2 values indicate better predictive accuracy. The Tandem Network achieves the highest R^2 scores for thickness (0.986) and periodicity (0.996), whereas for radius (0.996) the value is identical to 1D CNN. The comparison demonstrates that the Tandem Network generally provides superior performance in terms of both MAE and R^2 values across the different parameters.

between the predicted and actual values. In predicting thickness and periodicity, the tandem network exhibits slightly higher R^2 scores compared to the other two networks, while for radius, its score is similar to that of the 1D-CNN.

We further conduct accuracy analysis to assess the reliability and precision of our classification approach. For the classification problems concerning material identification and lattice arrangement, our model's accuracy converges to an impressive value close to 1, as depicted in Figure 5a. This signifies the model's adeptness in perfectly classifying among the three distinct materials and two lattice structures. This high accuracy underscores the robustness of our approach and its potential applicability in various material and structure recognition tasks.

Continuing from the robust accuracy of the retrieved geometrical values, we perform an additional validation step by utilizing the predicted parameters by the tandem network in FDTD simulations. These predicted structural parameters serve as inputs to generate transmission spectra, shown as the red curve in Figure 5b, and then compared with the desired transmission spectra (black curve) to confirm the effectiveness of our inverse network. This approach is extended to generate Figure 5c-5d and Figure S6 for different NHA structures. We observe a clear alignment between the target spectra and those obtained from the reconstructed dimensional parameters.

To verify the generalization ability, we test the tandem network with nanohole array spectra and geometries that are completely different from those in the training and test datasets (Supplementary Text 4). The comparison between original values and predicted values of thickness, radius, and periodicity is shown in Supplementary Figures S7 and S8. It is clear that the retrieved geometrical values from the tandem network are very close to the original values. Results from these studies indicate that the trained tandem network for inverse design is sufficiently reliable even outside the dataset.

3.3 Assessing the Effectiveness of Deep Neural Network for Nanohole Array Rapid Prototyping

Now that we have a fully developed deep-learning model available, we investigate its practical utility as a tool for rapidly prototyping the optical response of nanohole arrays. Using an experimental validation method, we aim to determine the efficacy of our deep neural network. For this purpose, we select a gold nanohole array on a glass substrate as our test case. The fabrication process involves deep-UV lithography, resulting in the creation of a gold nanohole array, as depicted in the scanning electron microscopy image shown in Figure 6b. The optical setup designed for collecting the transmission spectrum of the gold nanohole array is illustrated in Figure 6a. Employing a Nikon TE 2000-U inverted microscope coupled with an Ocean Optics HR4000 spectrometer, we obtain all spectral data. The system utilizes a normally incident dia-illumination unpolarized broadband light source, spanning from 400 to 1100 nm, to capture the transmission spectrum of the plasmonic nanohole array. This array's transmission signals are captured using a Nikon microscope objective (10×, NA =0.30), and the spectrometer records the data with a 100-ms integration time.

To test the neural network's performance against real-world data, we input geometric parameters to the forward model and transmission spectrum to the inverse model (tandem network). Importantly, these experimental datasets were not part of the training data. In the forward network, the model is fed the structural parameters (thickness, radius, and periodicity) as well as lattice and material information. The comparison between the predicted transmission spectrum and the experimental one is shown in Figure 6c, where the DNN-predicted spectrum (solid black curve) aligns closely with the experimentally measured one (dashed red curve). Additionally, we apply the inverse network to the measured spectra obtained from the fabricated nanohole array devices. Running these spectra through the inverse network and performing FDTD simulations with the predicted geometries

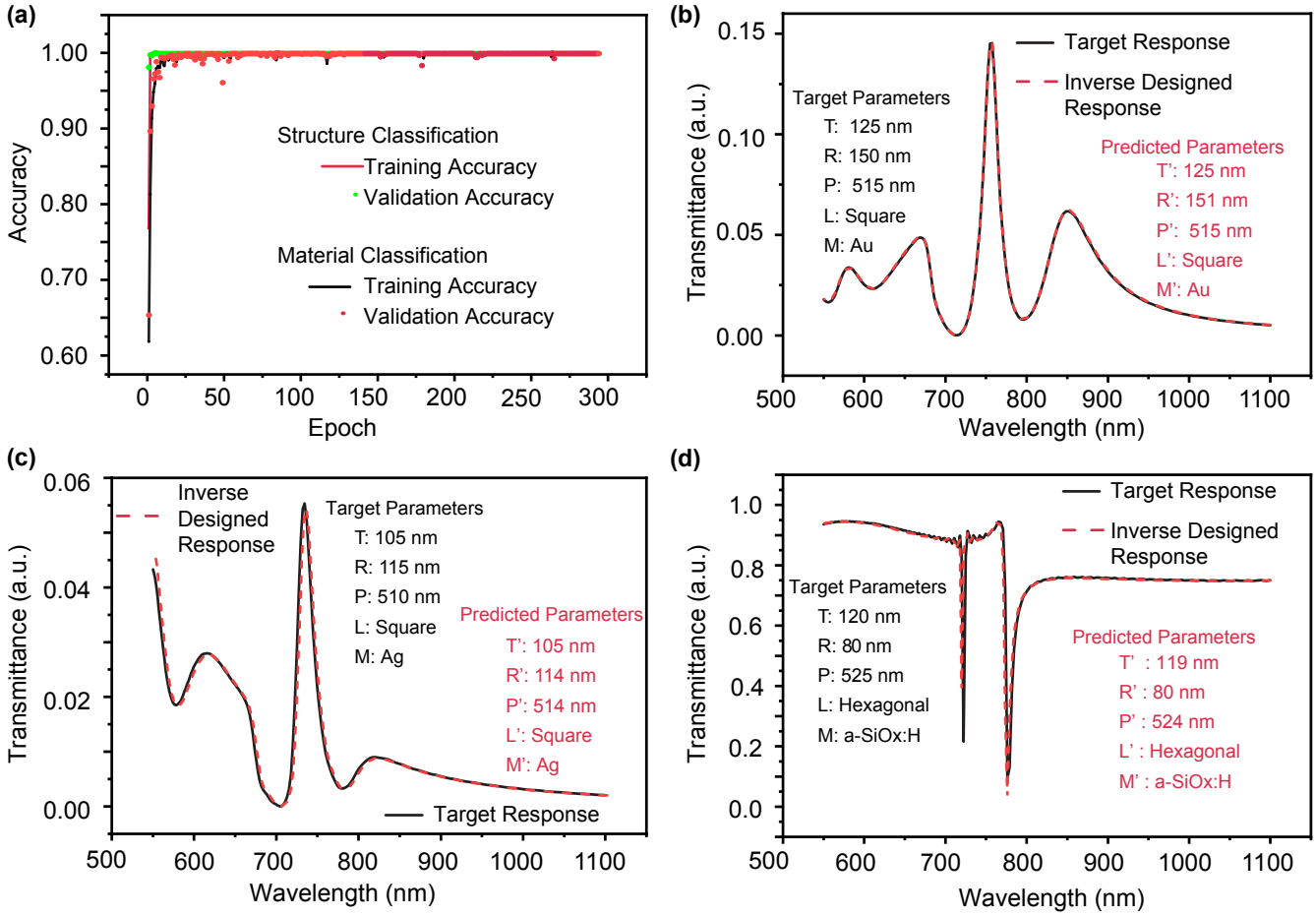

Fig. 5 Inverse design (tandem network) results for target spectra randomly selected from the test dataset. (a) Training and validation accuracy as a function of epoch for structure classification and material classification tasks. The plot shows the training accuracy and validation accuracy for both tasks, with accuracy values stabilizing around 1 after approximately 50 epochs. (b) Comparison of target response and inverse designed response for a square lattice with Au film. The target parameters are T: 125 nm, R: 150 nm, P: 515 nm, L: Square, and M: Au, where thickness, radius, periodicity, lattice, and film material are denoted by T, R, P, L, and M respectively. The predicted parameters are T': 125 nm, R': 151 nm, P': 515 nm, L: Square, and M: Au. (c) Comparison of target response and inverse designed response for a square lattice with Ag film. The target parameters are T: 105 nm, R: 115 nm, P: 510 nm, L: Square, and M: Ag. The predicted parameters are T': 105 nm, R': 114 nm, P': 514 nm, L': Square, and M': Ag. (d) Comparison of target response and inverse designed response for a hexagonal lattice with a-SiOx:H film. The target parameters are T: 120 nm, R: 80 nm, P: 525 nm, L: Hexagonal, and M: a-SiOx:H. The predicted parameters are T': 119 nm, R': 80 nm, P': 524 nm, L': Hexagonal, and M': a-SiOx:H. In all spectral plots (b), (c), and (d), the black solid curves represent the target transmittance spectra, while the red dashed lines represent the transmittance spectra predicted by conducting FDTD calculations using the predicted structural parameters.

yield results illustrated in Figure 6d. The observed agreement between the spectrum generated from DL-predicted geometry (solid black curve) and the experimentally acquired spectrum (dashed red curve) further supports the model's accuracy in predicting the geometrical parameters and optical response of nanohole arrays.

To explore the effect of about dataset size, we extend our dataset to 7260 samples (by extending the periodicity to 530 nm) and retrain our model. The performance improvements are marginal. Supplementary Table S6 compares the two dataset sizes, showing closely matched performance metrics with slight discrepancies. These discrepancies suggest that as the dataset size increases, hyperparameters such as the number of nodes, layers, and learning rate need to be optimized. We further evaluate the tandem neural network trained with 7260 samples using the same experimental data used for the evaluation of the network trained with 6655 samples. As shown in Supplementary Figure S10, predictions from the two datasets closely match each other. For the same target parameters, the predicted parameters are T': 121 nm, R': 142 nm, P': 520 nm, L': Square, M': Au. To gain more confidence in our model, we perform an additional validation using experimental data. Supplementary Figure S10b shows that our neural network predictions align well with the experimental spectrum. The target parameters are T: 120 nm, R: 140 nm, P: 530 nm, L: Square, M: Au. For the dataset size of 7260, the predicted parameters are T': 121 nm, R': 141 nm, P': 530 nm, L': Square, M': Au. These results demonstrate the reliability of our datasets and the model used for prediction.

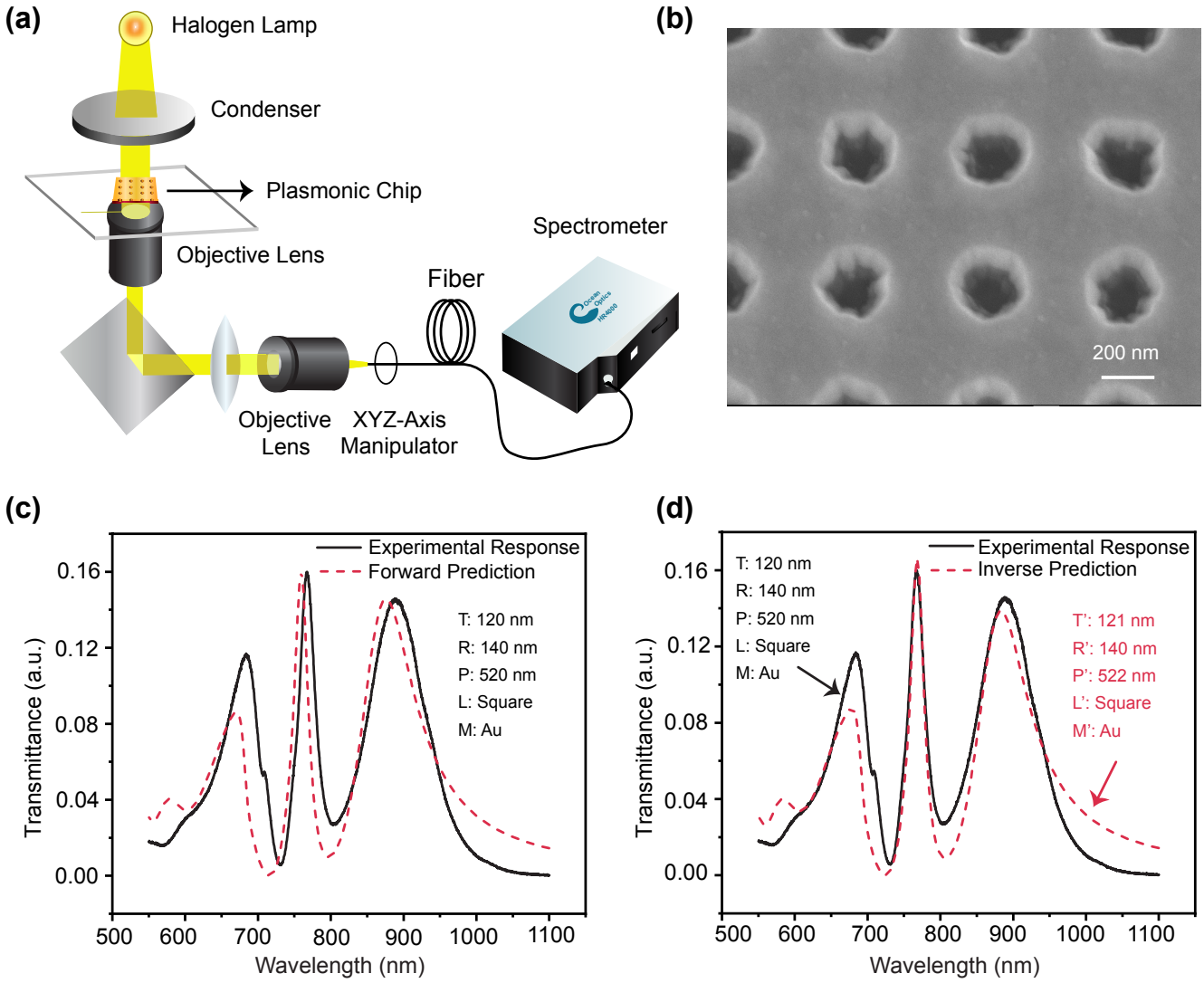

Fig. 6 Evaluation of forward and inverse model through comparing square Au NHA experimental data to DNN-predicted data. (a) Experimental setup for measuring transmission spectra. (b) SEM image of the fabricated Square Au NHA. (c) Experimentally measured transmission spectra (black solid lines) compared with DNN-predicted spectra (red dashed lines) for the forward model. The nanohole array parameters are specified as a square lattice with thickness (T) of 120 nm, radius (R) of 140 nm, and periodicity (P) of 520 nm. (d) Design parameters of NHA geometry derived based on the experimental transmission spectra by the inverse network (tandem). The predicted geometry is then fed into the Lumerical FDTD to produce a transmission spectrum. The experimental transmission spectrum is shown by the black solid line and the spectrum based on inverse predicted geometry is shown by the red dashed line. The target parameters are T: 120 nm, R: 140 nm, P: 520 nm, L: Square, M: Au, while the predicted parameters are T': 121 nm, R': 140 nm, P': 522 nm, L': Square, M': Au.

4 Conclusion

In this work, we've developed deep learning models to expedite the design of nanohole arrays, integrating multiple materials and array patterns. Our dataset for training the model was generated using Lumerical FDTD, with Optuna used to optimize the model hyperparameters. The remarkable precision of our forward model in predicting transmission spectra across diverse structural features highlights its potential as a potent alternative to time-consuming and computationally expensive electromagnetic simulation.

After comparing three different deep learning models for inverse design, we chose the tandem network for its lowest MAE and highest R^2 scores. This model accurately forecasts material attributes, lattice geometries, and structural parameters from transmission spectra substantially different from the training and test set. Furthermore, our deep learning results align well with both FDTD simulations and experimental data, demonstrating the reliability of our model.

Our current model precisely predicts nanohole array characteristics for Au, Ag, and a-SiOx:H arrays in hexagonal and square array configurations. However, it also holds potential for broader applications across a range of materials and types. By incorporating data from various materials and types into the model's training, it can serve as a versatile prediction tool for diverse nanohole arrays.

To design devices with superior performance beyond the limitations of the training set, several strategies can be employed.

First, incorporating a more diverse dataset with additional materials and configurations can enhance the model's predictive capabilities. Data augmentation techniques, such as adding noise or transformations, introduce diversity and improve generalization[47,48]. Active learning frameworks enable the model to select the most useful samples for labeling, continuously enhancing performance[49]. Additionally, generative models like GANs[50] and VAEs[51] can be used to explore new design spaces. For instance, Jiang and Fan showed that conditional GANs can efficiently learn the key features of meta-gratings and generalizes them for broader design exploration[52]. They incorporated adjoint variable calculations directly into the GAN framework. This allows them to rapidly generate new, high-performing designs that can even operate outside the parameters used for training. As a future scope generative networks can be used to inverse design NHA devices that will exhibit better performance from the training set.

Overall, this study paves the way for further exploration, particularly by expanding the model's repertoire to include data from a wider range of materials. This expanded scope would enable the model to predict the structure and optical properties of a wide range of nanohole arrays, providing a powerful tool for tailored design on demand. Our model's capability to integrate diverse lattice geometries and materials makes it suitable for various applications, including chemical and biosensors, surface-enhanced Raman spectroscopy, and solar cell applications.

Author Contributions

Tasnia Jahan: Data curation, Formal analysis, Software, Methodology, Validation, Writing - original draft, Writing - review & editing, Visualization. **Tomoshree Dash**: Methodology, Visualization, Software, Validation, Writing - review & editing. **Shifat E. Arman**: Formal analysis, Investigation, Writing - review & editing. **Reefat Inum**: Methodology, Formal analysis. **Sharnali Islam**: Formal analysis, Validation. **Lafifa Jamal**: Formal analysis, Funding acquisition. **Ahmet Ali Yanik**: Formal analysis, Project administration, Funding acquisition. **Ahsan Habib**: Conceptualization, Methodology, Writing - original draft, Writing - review & editing, Visualization, Project administration, Funding acquisition.

Data Availability

The datasets generated during the current study are available at GitHub Repository: https://github.com/ahsan-ucsc/DL-Assisted-NHA-Inverse-Design-.git.

Conflicts of interest

The authors declare that there are no conflicts of interest to declare.

Acknowledgements

Ahsan Habib and Lafifa Jamal acknowledge the funding provided by the Collaborative Research Grant, Faculty of Engineering and Technology, University of Dhaka. Ahmet Ali Yanik acknowledges support from the National Science Foundation [ECCS-1611290] and the National Science Foundation CAREER Award [ECCS-1847733]. Gold nanohole fabrication was conducted at the UCSB Nanofabrication Facility, an open-access laboratory. We would like to express our sincere gratitude to Biljana Stamenic and Demis D. John for their invaluable assistance with the fabrication process. Their expertise and support have been instrumental in the successful completion of this research.

Notes and references

1 T. W. Ebbesen, H. J. Lezec, H. Ghaemi, T. Thio and P. A. Wolff, *nature*, 1998, **391**, 667–669.
2 H. Ghaemi, T. Thio, D. e. a. Grupp, T. W. Ebbesen and H. Lezec, *Physical review B*, 1998, **58**, 6779.
3 S. P. Sahu, A. Mahigir, B. Chidester, G. Veronis and M. R. Gartia, *Nano letters*, 2019, **19**, 6192–6202.
4 A. A. Yanik, M. Huang, O. Kamohara, A. Artar, T. W. Geisbert, J. H. Connor and H. Altug, *Nano letters*, 2010, **10**, 4962–4969.
5 R. Bartholomew, C. Williams, A. Khan, R. Bowman and T. Wilkinson, *Optics Letters*, 2017, **42**, 2810–2813.
6 J. A. Jackman, E. Linardy, D. Yoo, J. Seo, W. B. Ng, D. J. Klemme, N. J. Wittenberg, S.-H. Oh and N.-J. Cho, *Small*, 2016, **12**, 1159–1166.
7 A. E. Cetin, P. Iyidogan, Y. Hayashi, M. Wallen, K. Vijayan, E. Tu, M. Nguyen and A. Oliphant, *ACS sensors*, 2018, **3**, 561–568.
8 A. A. Yanik, A. E. Cetin, M. Huang, A. Artar, S. H. Mousavi, A. Khanikaev, J. H. Connor, G. Shvets and H. Altug, *Proceedings of the National Academy of Sciences*, 2011, **108**, 11784–11789.
9 J.-C. Yang, J. Ji, J. M. Hogle and D. N. Larson, *Nano letters*, 2008, **8**, 2718–2724.
10 D. Conteduca, I. Barth, G. Pitruzzello, C. P. Reardon, E. R. Martins and T. F. Krauss, *Nature communications*, 2021, **12**, 3293.
11 H. Im, N. C. Lindquist, A. Lesuffleur and S.-H. Oh, *ACS nano*, 2010, **4**, 947–954.
12 A. Barik, L. M. Otto, D. Yoo, J. Jose, T. W. Johnson and S.-H. Oh, *Nano letters*, 2014, **14**, 2006–2012.
13 M. L. Tseng, Y. Jahani, A. Leitis and H. Altug, *Acs Photonics*, 2020, **8**, 47–60.
14 Y. LeCun, Y. Bengio and G. Hinton, *Nature*, 2015, **521**, 436–444.
15 W. Ma, Z. Liu, Z. A. Kudyshev, A. Boltasseva, W. Cai and Y. Liu, *Nature Photonics*, 2021, **15**, 77–90.
16 Q. Li, H. Fan, Y. Bai, Y. Li, M. Ikram, Y. Wang, Y. Huo and Z. Zhang, *New Journal of Physics*, 2022, **24**, 063005.
17 Y. Li, Y. Wang, S. Qi, Q. Ren, L. Kang, S. D. Campbell, P. L. Werner and D. H. Werner, *IEEE Access*, 2020, **8**, 139983–139993.
18 Z. Li, R. Pestourie, Z. Lin, S. G. Johnson and F. Capasso, *ACS Photonics*, 2022, **9**, 2178–2192.
19 S. An, C. Fowler, B. Zheng, M. Y. Shalaginov, H. Tang, H. Li, L. Zhou, J. Ding, A. M. Agarwal, C. Rivero-Baleine *et al.*, *ACS Photonics*, 2019, **6**, 3196–3207.
20 L. Pilozzi, F. A. Farrelly, G. Marcucci and C. Conti, *Communications Physics*, 2018, **1**, 57.

21 T. Zhang, J. Wang, Q. Liu, J. Zhou, J. Dai, X. Han, Y. Zhou and K. Xu, *Photonics Research*, 2019, **7**, 368–380.

22 Y. Chen, J. Zhu, Y. Xie, N. Feng and Q. H. Liu, *Nanoscale*, 2019, **11**, 9749–9755.

23 I. Malkiel, M. Mrejen, A. Nagler, U. Arieli, L. Wolf and H. Suchowski, *Light: Science & Applications*, 2018, **7**, 60.

24 J. Peurifoy, Y. Shen, L. Jing, Y. Yang, F. Cano-Renteria, B. G. DeLacy, J. D. Joannopoulos, M. Tegmark and M. Soljačić, *Science advances*, 2018, **4**, eaar4206.

25 W. Ma, F. Cheng and Y. Liu, *ACS nano*, 2018, **12**, 6326–6334.

26 R. Lin, Y. Zhai, C. Xiong and X. Li, *Optics Letters*, 2020, **45**, 1362–1365.

27 X. Liao, L. Gui, Z. Yu, T. Zhang and K. Xu, *Optical Materials Express*, 2022, **12**, 758–771.

28 J. Ma, Y. Huang, M. Pu, D. Xu, J. Luo, Y. Guo and X. Luo, *Journal of Physics D: Applied Physics*, 2020, **53**, 464002.

29 D. Liu, Y. Tan, E. Khoram and Z. Yu, *Acs Photonics*, 2018, **5**, 1365–1369.

30 L. Gao, X. Li, D. Liu, L. Wang and Z. Yu, *Advanced Materials*, 2019, **31**, 1905467.

31 S. So, J. Mun and J. Rho, *ACS applied materials & interfaces*, 2019, **11**, 24264–24268.

32 J. Kim, B. Neseli, J.-y. Kim, J. Yoon, H. Yoon, H.-H. Park and H. Kurt, *Optics Express*, 2023, **31**, 2049–2060.

33 C. Liu, J. Zhang, Y. Zhao and B. Ai, *Advanced Intelligent Systems*, 2023, **5**, 2300121.

34 A.-P. Blanchard-Dionne and M. Meunier, *Nanophotonics*, 2018, **8**, 325–329.

35 Z. Zuo, Y. Wen and S. Zhang, *Nanoscale*, 2018, **10**, 14039–14046.

36 J. R. Ong, H. S. Chu, V. H. Chen, A. Y. Zhu and P. Genevet, *Optics letters*, 2017, **42**, 2639–2642.

37 P. B. Johnson and R. W. Christy, *Physical Review B*, 1972, **6**, 4370–4379.

38 E. D. Palik, *Handbook of optical constants of solids*, Academic press, 1998, vol. 3.

39 F. Chollet *et al.*, *see https://keras. io "*, 2015.

40 S. Verma, S. Chugh, S. Ghosh and B. A. Rahman, *Scientific Reports*, 2023, **13**, 1129.

41 A. Estrada-Real, A. Khaireh-Walieh, B. Urbaszek and P. R. Wiecha, *Photonics and Nanostructures-Fundamentals and Applications*, 2022, **52**, 101066.

42 I. Tanriover, W. Hadibrata and K. Aydin, *Acs Photonics*, 2020, **7**, 1957–1964.

43 T. Ma, M. Tobah, H. Wang and L. J. Guo, *Opto-Electronic Science*, 2022, **1**, 210012–1.

44 Y. Yoo, *Knowledge-Based Systems*, 2019, **178**, 74–83.

45 T. Akiba, S. Sano, T. Yanase, T. Ohta and M. Koyama, Proceedings of the 25th ACM SIGKDD international conference on knowledge discovery & data mining, 2019, pp. 2623–2631.

46 N. Srivastava, G. Hinton, A. Krizhevsky, I. Sutskever and R. Salakhutdinov, *The journal of machine learning research*, 2014, **15**, 1929–1958.

47 A. Krizhevsky, I. Sutskever and G. E. Hinton, *Communications of the ACM*, 2017, **60**, 84–90.

48 T. He, Z. Zhang, H. Zhang, Z. Zhang, J. Xie and M. Li, Proceedings of the IEEE/CVF conference on computer vision and pattern recognition, 2019, pp. 558–567.

49 Y. Gal, R. Islam and Z. Ghahramani, International conference on machine learning, 2017, pp. 1183–1192.

50 I. Goodfellow, J. Pouget-Abadie, M. Mirza, B. Xu, D. Warde-Farley, S. Ozair, A. Courville and Y. Bengio, *Communications of the ACM*, 2020, **63**, 139–144.

51 D. P. Kingma and M. Welling, *arXiv preprint arXiv:1312.6114*, 2013.

52 J. Jiang and J. A. Fan, *Nano Letters*, 2019, **19**, 5366–5372.

The dataset generated and analyzed during the current study, including structural parameters and transmission spectra, is available at Github at https://github.com/ahsan-ucsc/NHA-Inverse-Design.git . Additionally, the code used for training the deep learning models and performing the simulations is also available at the same repository.